Chapter 10

Fano Resonance in High-Permittivity Objects

Xianghong Kong, Lina Qiu and Gaobiao Xiao

Additional information is available at the end of the chapter

http://dx.doi.org/10.5772/intechopen.70518

Abstract

In this chapter, Fano resonances in simple structures with high permittivity such as spheres or core-shell particles are analyzed by Mie theory. The Mie scattering coefficients can be decomposed into slow varying backgrounds and narrow resonances, which cause the Fano resonances in scattered field. For structures of arbitrary shapes, temporal coupled-mode theory is applied to explain the Fano resonances found in the scattering cross section. At last, we analyze the periodic structures by using band diagram, and it shows that the Fano resonances can be viewed as the superposition of the Bloch wave and the Mie scattering wave.

Keywords: Fano resonance, Mie theory, temporal coupled-mode theory, photonic crystal, sensor

1. Introduction

Fano resonance was first discovered in quantum systems to describe the asymmetrically shaped ionization spectral lines of atoms [1]. The asymmetric profile is caused by the interference between a broad background state and a narrow discrete state. The interference phenomenon also exists in electromagnetic system and was first observed by Wood [2]. With the development of metamaterials, Fano resonances have been observed in many classical oscillator systems, such as nonconcentric ring/disk cavities [3], asymmetric split rings, and dolmen structures [4]. Such Fano systems are caused by symmetry breaking of the geometry and are usually consisted of metal and dielectric. Recently, metamaterials composed of high refractive index materials have attracted researchers' attentions since they can enhance efficiency significantly [5]. Fano resonances occur in these metamaterials usually have larger quality factor since metal is replaced by lossless high-permittivity dielectric, which makes Fano curve sharper compared with conventional metamaterials.

In this chapter, we will investigate the Fano resonances in high-permittivity objects theoretically and do the simulations to verify the accuracy of theories, which will provide a guidance for the further study and applications. The chapter is organized as follows:

In the second section, we analyze the Fano resonances in high-permittivity spheres, which are the simplest structures that can be analyzed by applying Mie theory easily.

In the third section, we will use the Mie theory to investigate the Fano resonances in core-shell particles. With more degrees of freedom for design, core-shell structures are more suitable for applications such as sensors.

In the fourth section, a new method called temporal coupled-mode theory (TCMT) is used to explain the Fano resonances found in high permittivity arbitrarily shaped objects. Combined with cylindrical wave expansion (2D) or spherical wave expansion (3D), we can use TCMT to model the Fano resonances in scattering by an arbitrary object.

In the fifth section, we do some numerical simulation on periodic array of cylinders and show that Fano resonances can be observed in transmission spectra as a result of interference of leaky guided modes of cylinders with an incident electromagnetic wave.

In the last section, we will draw a conclusion briefly.

2. Fano resonances in high-permittivity spheres

2.1. Mie theory

Mie scattering was first discovered by Mie in 1908 [6]. In spite of the long history, Mie theory still governs the forefront optical devices such as nanoantennas [7] and metamaterials [8]. It describes the scattering of a plane wave by a homogeneous sphere. The solution takes form of an infinite series of spherical multipole partial waves. For different electromagnetic modes, the positions of resonances which can be calculated by Mie theory are different. Resonance arises when the incident wave reaches an eigenmode frequency and excites localized modes in the sphere.

Let us assume the radius of sphere is a. The relative permittivities and permeabilities of sphere ($r \le a$) and embedding medium ($r > a$) are (ϵ_1, μ_1) and (ϵ, μ), respectively. The Mie scattering coefficients are [6]:

$$a_n = \frac{\mu_1 x j_n(x)\left[m x j_n(mx)\right]' - \mu m^2 x j_n(mx)\left[x j_n(x)\right]'}{-\mu_1 x h_n^{(1)}(x)\left[m x j_n(mx)\right]' + \mu m^2 x j_n(mx)\left[x h_n^{(1)}(x)\right]'} \tag{1}$$

$$b_n = \frac{\mu x j_n(x)\left[m x j_n(mx)\right]' - \mu_1 x j_n(mx)\left[x j_n(x)\right]'}{-\mu x h_n^{(1)}(x)\left[m x j_n(mx)\right]' + \mu_1 x j_n(mx)\left[x h_n^{(1)}(x)\right]'} \tag{2}$$

where $x = ka$ ($k = \omega/c$ is the wavenumber of incident wave) is the size parameter of the sphere,

and $m = \sqrt{\frac{\epsilon_1 \mu_1}{\epsilon \mu}}$ is the relative refractive index. $j_n(x)$ and $h_n^{(1)}(x)$ stand for spherical Bessel functions and Hankel functions of the first kind, respectively.

2.2. Decomposition of Mie scattering coefficients

For simplicity, the embedding medium is considered to be vacuum in the following analysis, so we have $\epsilon = 1$, $\mu = 1$. We assume the relative permeability of sphere to be 1 and the relative permittivity ϵ_1 to be a purely real number, so the relative refractive index $m = \sqrt{\epsilon_1}$. Eq. (1), which represents electric scattering coefficients can be rewritten by

$$a_n = -\frac{\left[xj_n(x)\right]'}{\left[xh_n^{(1)}(x)\right]'} + \frac{\frac{i}{\left[xh_n^{(1)}(x)\right]'^2}}{\frac{\epsilon_1 xj_n\left(\sqrt{\epsilon_1}x\right)}{\left[\sqrt{\epsilon_1}xj_n\left(\sqrt{\epsilon_1}x\right)\right]'} - \frac{xh_n^{(1)}(x)}{\left[xh_n^{(1)}(x)\right]'}} \tag{3}$$

where $-\left[xj_n(x)\right]'/\left[xh_n^{(1)}(x)\right]'$ means a slow varying background and $\frac{i}{\left[xh_n^{(1)}(x)\right]'^2}/\left(\frac{\epsilon_1 xj_n\left(\sqrt{\epsilon_1}x\right)}{\left[\sqrt{\epsilon_1}xj_n\left(\sqrt{\epsilon_1}x\right)\right]'} - \frac{xh_n^{(1)}(x)}{\left[xh_n^{(1)}(x)\right]'}\right)$ means a narrow resonance when high-permittivity dielectric sphere is considered [9].

As shown in **Figure 1**, squared norm of Mie coefficient $|a_1|^2$ is plotted when $\epsilon_1 = 1000$. It can be described by superposition of narrow resonance and slow varying background.

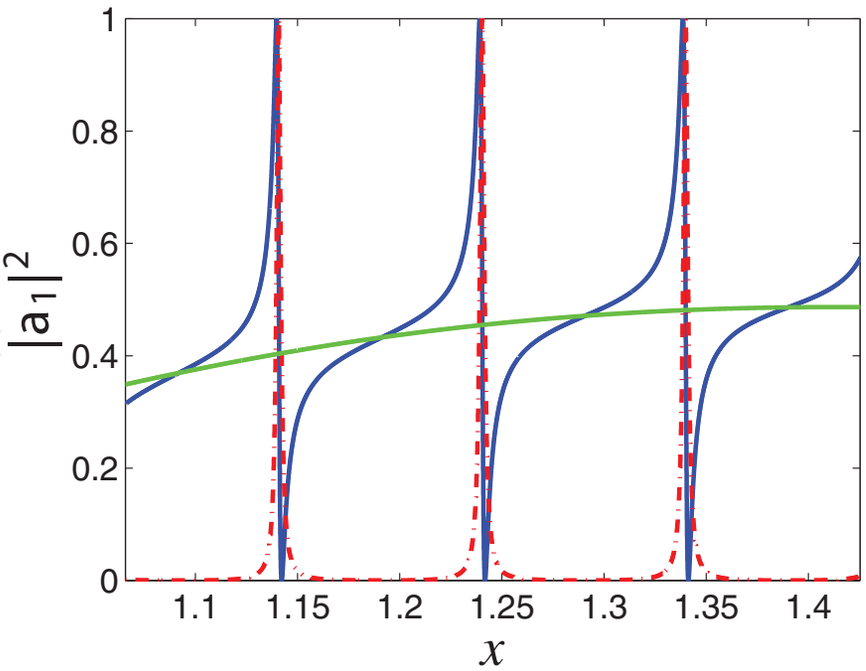

Figure 1. Squared norm of Mie coefficient $|a_1|^2$ (blue curve), slow varying background $\left|\frac{\left[xj_1(x)\right]'}{\left[xh_1^{(1)}(x)\right]'}\right|^2$ (green curve), and narrow resonance (red dot-dash line) for a sphere with $\epsilon_1 = 1000$.

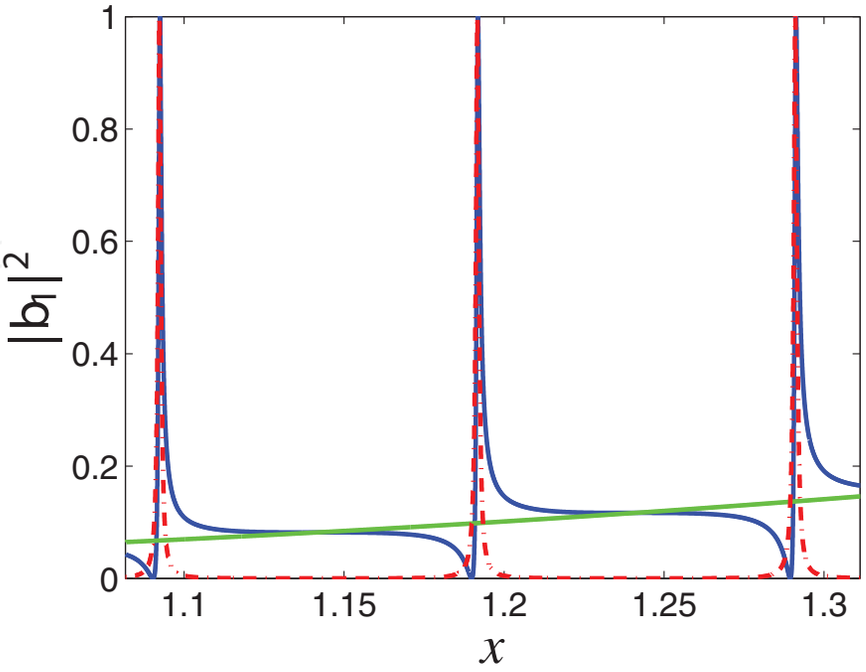

Figure 2. Squared norm of Mie coefficient $|b_1|^2$ (blue curve), slow varying background $\left|\frac{j_1(x)}{h_1^{(1)}(x)}\right|^2$ (green curve), and narrow resonance (red dot-dash line) for a sphere with $\epsilon_1 = 1000$.

Similarly, magnetic scattering coefficient $|b_n|$ can be decomposed into two parts:

$$b_n = -\frac{j_n(x)}{h_n^{(1)}(x)} + \frac{\frac{-i}{\left[xh_n^{(1)}(x)\right]^2}}{\frac{\left[\sqrt{\epsilon_1}xj_n\left(\sqrt{\epsilon_1}x\right)\right]'}{xj_n\left(\sqrt{\epsilon_1}x\right)} - \frac{\left[xh_n^{(1)}(x)\right]'}{xh_n^{(1)}(x)}} \tag{4}$$

where $-j_n(x)/h_n^{(1)}(x)$ represents a slow varying background and $\frac{-i}{\left[xh_n^{(1)}(x)\right]^2} / \left(\frac{\left[\sqrt{\epsilon_1}xj_n\left(\sqrt{\epsilon_1}x\right)\right]'}{xj_n\left(\sqrt{\epsilon_1}x\right)} - \frac{\left[xh_n^{(1)}(x)\right]'}{xh_n^{(1)}(x)}\right)$ represents a narrow resonance (as shown in **Figure 2**).

The slow varying backgrounds are the same as scattering coefficients of PEC spheres.

2.3. Rewrite Mie coefficients in the form of Fano function

Normalized Fano function can be expressed as $\frac{1}{1+q^2}\frac{\left(q+\frac{x-x_0}{\Gamma}\right)^2}{1+\left(\frac{x-x_0}{\Gamma}\right)^2}$, where x_0, Γ, and q represent resonance position, resonance width, and Fano parameter, respectively. Compared with conventional Lorentz resonance, Fano resonance will exhibit asymmetric line shape and usually has sharper resonant curve.

When the permittivity of sphere is high, we can rewrite the Mie coefficients in the form of Fano function. The resonance position, resonance width, and Fano parameter can be achieved by following Eqs. (10):

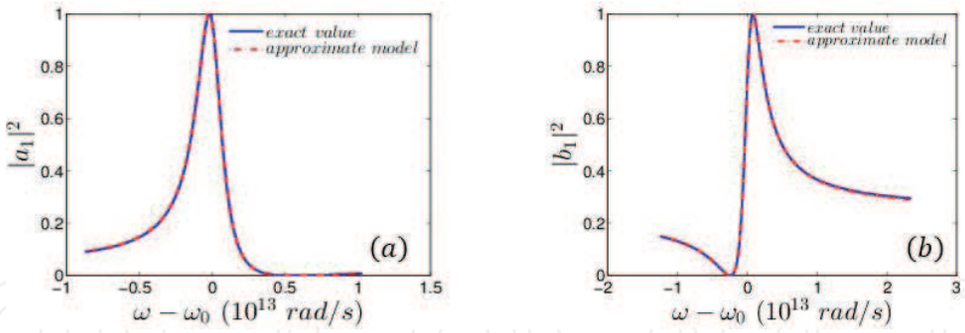

Figure 3. The exact value of Mie scattering coefficients (blue line) and Fano curve predicted by approximate model (red dot-dash line) are shown for (a) electric dipole $|a_1|^2$ when $\omega_0 = 3 \times 10^{15}$ *rad/s* , $a = 64.33$ *nm* , $\epsilon_1 = 1000$ and (b) magnetic dipole $|b_1|^2$ when $\omega_0 = 3 \times 10^{15}$ *rad/s* , $a = 148.97$ *nm* , $\epsilon_1 = 1000$.

$$\frac{\epsilon_1 x_0 j_n\left(\sqrt{\epsilon_1} x_0\right)}{\left[\sqrt{\epsilon_1} x_0 j_n\left(\sqrt{\epsilon_1} x_0\right)\right]'} = Re\left(\frac{x_0 h_n^{(1)}(x_0)}{\left[x_0 h_n^{(1)}(x_0)\right]'}\right) \tag{5}$$

$$\mathrm{q} = \frac{\left[x_0 y_n(x_0)\right]'}{\left[x_0 j_n(x_0)\right]'} sign\left(\frac{Im\left(\frac{x_0 h_n^{(1)}(x_0)}{\left[x_0 h_n^{(1)}(x_0)\right]'}\right)}{\left.\frac{\partial \frac{\epsilon_1 x j_n\left(\sqrt{\epsilon_1} x\right)}{\left[\sqrt{\epsilon_1} x j_n\left(\sqrt{\epsilon_1} x\right)\right]'}}{\partial \omega}\right|_{\omega=\omega_0}}\right) \tag{6}$$

$$\Gamma = \left|\frac{Im\left(\frac{x_0 h_n^{(1)}(x_0)}{\left[x_0 h_n^{(1)}(x_0)\right]'}\right)}{\left.\frac{\partial \frac{\epsilon_1 x j_n\left(\sqrt{\epsilon_1} x\right)}{\left[\sqrt{\epsilon_1} x j_n\left(\sqrt{\epsilon_1} x\right)\right]'}}{\partial \omega}\right|_{\omega=\omega_0}}\right| \tag{7}$$

In Eqs. (5)–(7), Re(x) and Im(x) mean the real and imaginary part of x, $y_n(x)$ represent the spherical Neumann functions, sign(x) denotes the sign function. These equations are the rewrite of electric scattering coefficients. Similarly, magnetic scattering coefficients can also be rewritten in the form of Fano function [10].

As shown in **Figure 3**, the approximate model which can be written in the form of Fano function matches well with the exact Mie scattering coefficient.

3. Fano resonances in core-shell particles with high-permittivity covers

In most researches [11, 12], Fano resonances observed in coated spheres are derived in the Rayleigh limit. However, the approximation may suffer a loss of precision when frequency gets higher. An exact analysis based on Mie theory is proposed to analyze Fano resonances by coated spheres with high-permittivity covers in a precise way [13].

3.1. Theoretical analysis

Let us assume the inner radius of core-shell particle is a_1 and the outer radius is a. The ratio of a_1 and a can be denoted as $\eta = a_1/a$. The relative permittivities and permeabilities of core ($0 < r \leq a_1$), shell ($a_1 < r \leq a$), and embedding medium ($r > a$) are (ϵ_1, μ_1), (ϵ_2, μ_2), and (ϵ_0, μ_0), respectively. The solution of scattering by coated spheres can be described by Mie theory. For simplicity, the embedding medium is considered to be vacuum in the following analysis which means $\epsilon_0 = 1$, $\mu_0 = 1$. Also, we assume $\mu_1 = \mu_2 = 1$, which means both core and shell are nonmagnetic. When the core-shell particles are covered by high-permittivity dielectric shells, we can decompose the scattering coefficients c_n^{TM} and c_n^{TE} into slow varying backgrounds and narrow resonances, which are similar to the high-permittivity spheres. For electric scattering coefficients, we have

$$c_n^{TM} = s_n^{TM} + r_n^{TM} \tag{8}$$

where

$$s_n^{TM} = -\frac{\left[xj_n(x)\right]'}{\left[xh_n^{(1)}(x)\right]'} \tag{9}$$

$x = k_0 a$ is the size parameter of outer sphere. s_n^{TM} represents the slow varying background and its expression is given in Eq. (9). As we can see, the background is the same as the electric scattering coefficient of a PEC sphere with radius a. r_n^{TM} represents the narrow resonance, and it can be calculated formally by subtracting s_n^{TM} from c_n^{TM}. The expression for narrow resonance can be found in [13].

Similarly, we can decompose magnetic scattering coefficients into two parts:

$$c_n^{TE} = s_n^{TE} + r_n^{TE} \tag{10}$$

where

$$s_n^{TE} = -\frac{j_n(x)}{h_n^{(1)}(x)} \tag{11}$$

As shown in **Figure 4**, the scattering coefficients can be viewed as the cascade of Fano resonances.

3.2. Application of sensors

Due to the sharp resonances near the resonance frequencies, Fano resonances have great potential applications in sensing problems [14–16]. Although some of them may have high sensitivity, the structures which are designed to produce Fano resonances are usually complicated and cannot be analyzed by formula exactly. Because of the simple structure, core-shell particles have the potential to be a great platform for sensing since they can be fabricated easily. In fact, core-shell particles consisted of metal and dielectric, can exhibit Fano resonances due to the

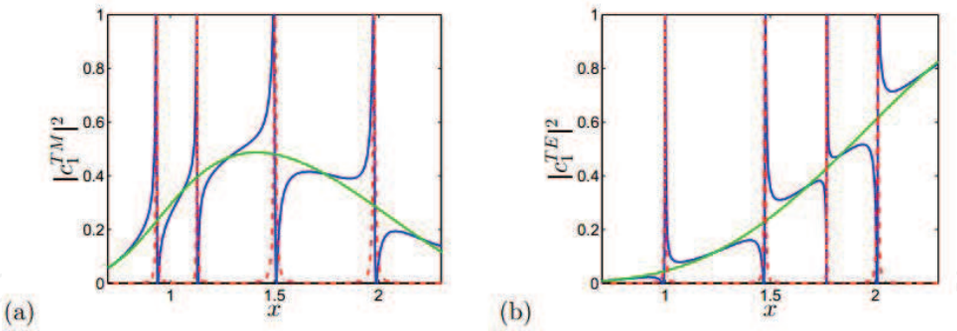

Figure 4. Squared norm of Mie coefficient (a) $|c_1^{TM}|^2$ (blue curve), slow varying background $\left|\frac{[xj_1(x)]'}{[xh_1^{(1)}(x)]'}\right|^2$ (green curve) and narrow resonances (red dot-dash line) (b) $|c_1^{TE}|^2$ (blue curve), slow varying background $\left|\frac{j_1(x)}{h_1^{(1)}(x)}\right|^2$ (green curve), and narrow resonances (red dot-dash line) for a core-shell particle with $a = 100\ nm$, $a_1 = 80\ nm$, $\epsilon_1 = 10$, $\epsilon_2 = 1000$.

hybridization between the plasmon resonances of the core and shell [17, 18]. However, the loss in metal may flatten the shape of Fano curve, which affects the sensitivity of Fano resonance sensor. Hence, we use lossless high-permittivity dielectric to replace the metal.

For the high-permittivity shell sensors, we can fill the core with unknown materials. The permittivity of the unknown material can be varied continuously such as liquid solvents. By detecting the scattering field over a discrete set of frequencies near Fano resonance position, we can achieve the permittivity we want with high accuracy.

The sensitivity for Fano resonance sensing can be examined by comparing the changes in the scattering coefficients between core-shell structure with high-permittivity shell and homogeneous sphere when the permittivity of material changes. We can define the sensitivity as an analogy to [14]

$$S_n^{TM} = \lim_{\Delta\epsilon \to 0} \frac{\Delta\left|c_n^{TM}\right|^2}{\Delta\epsilon} \tag{12}$$

As shown in **Figure 5(a)**, the difference of sensitivity between core-shell structure and sphere is plotted. As for the core-shell structure, the relative permittivity of core is increased by $\Delta\epsilon_1 = 0.1$. The maximum value of $\Delta\left|c_1^{TM}\right|^2$ occurs at $x = 0.49495$ (located by a vertical blue line) when $0.493 \le x \le 0.496$, which is $\Delta\left|c_1^{TM}\right|^2 = 0.1971$. In order to make a comparison with Fano resonance sensor, we figure out the scattering coefficients of a sphere with different permittivities as given for the core in core-shell structure. As shown in **Figure 5(b)**, the maximum value $\Delta\left|c_1^{TM}\right|^2 = 4.2259 \times 10^{-5}$ occurs at $x = 0.496$, which shows that the Fano resonance sensor offers a high sensitivity.

Since Fano resonances of high permittivity core-shell particles mentioned above only exist in scattering coefficients of multipole partial waves, it is difficult to achieve these coefficients separately by measuring the electromagnetic field distribution around the scatterers. In fact, by choosing operating frequency range properly, we can achieve the scattering coefficient of a

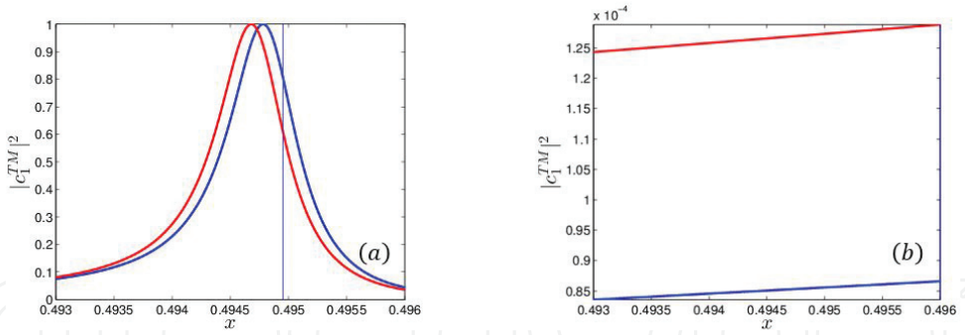

Figure 5. (a) $\left|c_1^{TM}\right|^2$ as a function of x for core-shell structure with different core permittivities ϵ_1 = 1.4 (blue line) and ϵ_1 = 1.5 (red line), high-permittivity shell ϵ_2 = 1000 , η = 0.8. (b) $\left|c_1^{TM}\right|^2$ as a function of x for sphere structure with ϵ_1 = 1.4 (blue line) and ϵ_1 = 1.5 (red line).

single partial wave ($c_1^{TM}$for example) without filtering out from the total electromagnetic fields. When size parameter x is small, most of the scattering coefficients c_n^{TM}, c_n^{TE} are zero, except for several coefficients with small n. We choose the first resonance frequency of c_1^{TM} as the operating frequency. Since Fano resonance is usually sharp and narrow, we find that overlap between different modes can be avoided if the frequency range narrows down. To explain it explicitly, we define the scattering cross section as [19]

$$Q_{sca} = \frac{2}{x^2}\sum_{n=1}^{\infty}(2n+1)\left(\left|c_n^{TM}\right|^2 + \left|c_n^{TE}\right|^2\right) \tag{13}$$

The contribution of c_1^{TM} to Eq. (13) can be defined as

$$Q_1^{TM} = \frac{6}{x^2}\left|c_1^{TM}\right|^2 \tag{14}$$

As shown in **Figure 6**, when we choose the first Fano resonance position of c_1^{TM} as the operating frequency, we find that the scattering cross section of multipole partial waves is the same as the scattering cross section of c_1^{TM} for a narrow frequency range. As shown in **Figure 6(a)**, Fano resonance can also be observed in scattering cross section which can be used to sense the permittivity.

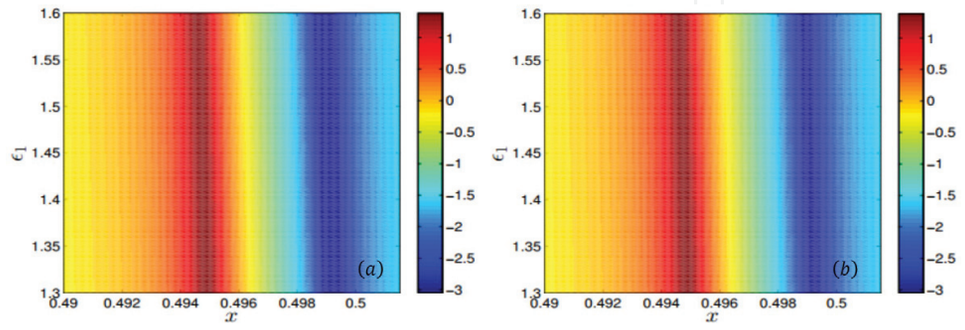

Figure 6. For the core-shell particle with high-permittivity shell ϵ_2 = 1000, η = 0.8, (a) $log_{10}(Q_{sca})$ is plotted as a function of x and ϵ_1 when the summation in Eq. (13) is truncated to n = 5. (b) $log_{10}\left(Q_1^{TM}\right)$ (calculated by Eq. (14)) is plotted as a function of x and ϵ_1.

The asymmetry parameter $\langle \cos\Theta \rangle$ is defined as the average cosine of the scattering angle Θ. For a spherical particle, the asymmetry parameter can be calculated by [20]

$$\langle \cos\Theta \rangle = \frac{4\pi}{x^2 Q_{sca}} Re\left(\sum_{n=1}^{\infty}\left(\frac{n(n+2)}{n+1}\left[c_n^{TM}\left(c_{n+1}^{TM}\right)^* + c_n^{TE}\left(c_{n+1}^{TE}\right)^*\right]\right)\right) + \frac{4\pi}{x^2 Q_{sca}} Re\left(\sum_{n=1}^{\infty}\left(\frac{2n+1}{n(n+1)}\left[c_n^{TM}\left(c_n^{TE}\right)^*\right]\right)\right) \tag{15}$$

The asymmetry parameter is positive if the particle scatters more light toward the forward direction while it is negative if more light is scattered toward the backscattering direction.

As shown in **Figure 7**, the width between maximum and minimum for a fixed core permittivity ϵ_1 narrows down compared with scattering cross section which is shown in **Figure 6**. With the increase of size parameter x, the asymmetry parameter reaches its maximum and decreases sharply to its minimum.

To check the average scattering direction changes from front to back, we use numerical simulation software COMSOL 5.0 to simulate the scattering of a plane wave by a core-shell

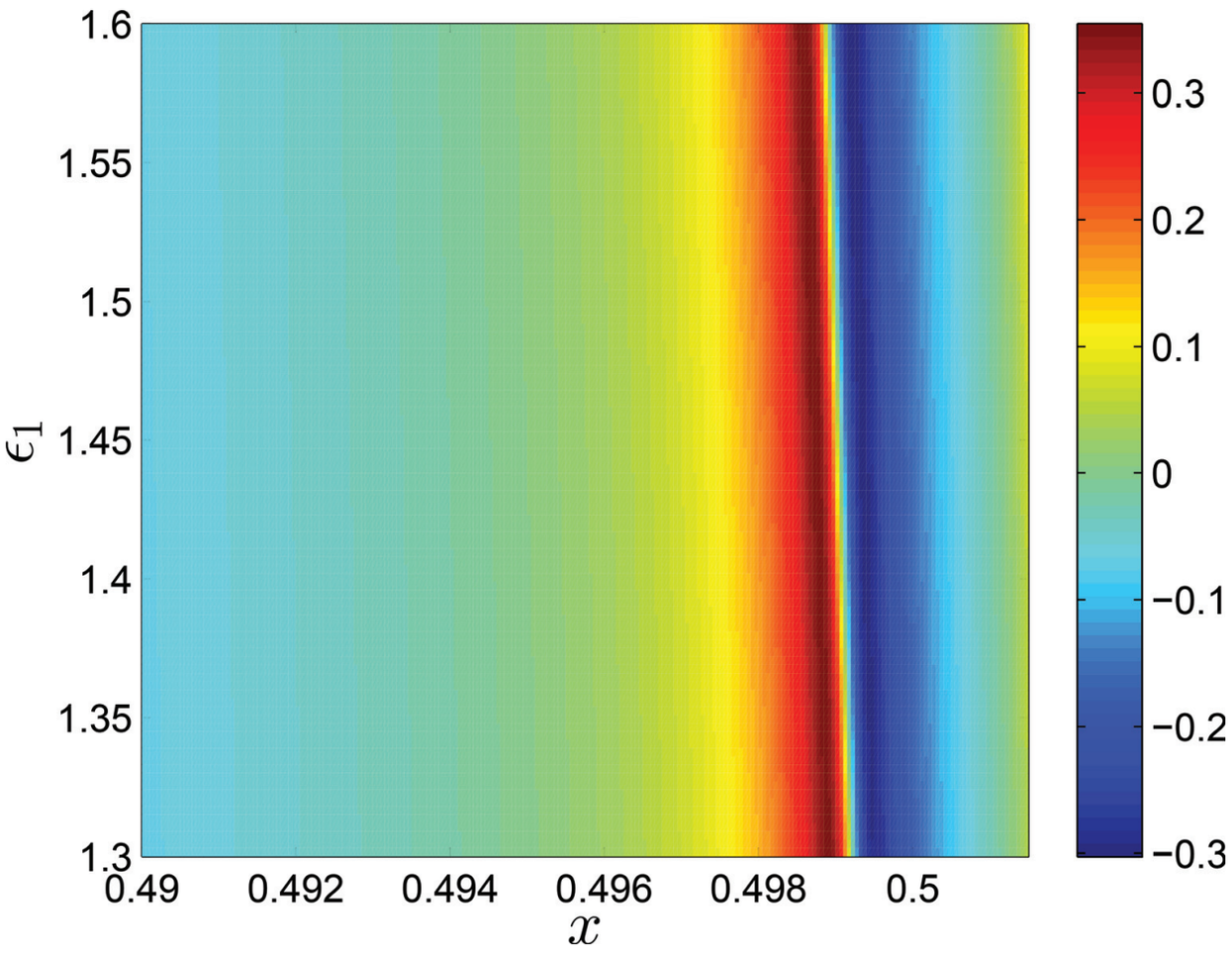

Figure 7. The asymmetry parameters for high-permittivity shell particles with $\epsilon_2 = 1000$, $\eta = 0.8$.

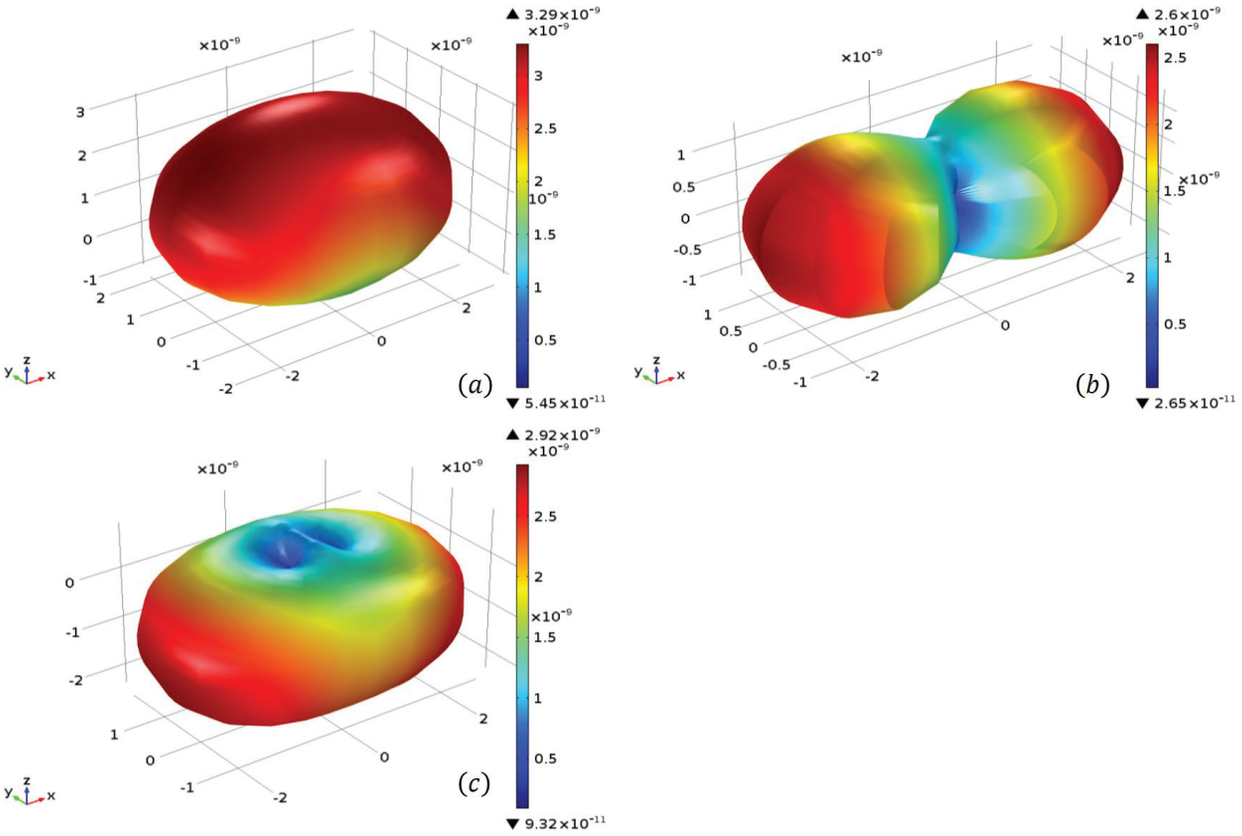

Figure 8. Scattering pattern of a high-permittivity shell particle with $\epsilon_2 = 1000$, $\epsilon_1 = 1.5$, $\eta = 0.8$, $a = 100\ nm$ when (a) $x = 0.498672$ (b) $x = 0.498980$ (c) $x = 0.499276$.

structure. The incident wave travels in the +z-direction and the electric field is oriented in the x-direction. Draw a horizontal line at $\epsilon_1 = 1.5$ in **Figure 7**, and we can find the average cosine of the scattering angle $\langle cos\Theta \rangle$ has a lineshape of Fano resonance as a function of size parameter x. As shown in **Figure 8(a)**, the high-permittivity shell structure scatters more light to the forward direction at $x = 0.498672$. When x increases, the asymmetry parameter decreases sharply from positive value to negative value. The minimum value is achieved at $x = 0.499276$ and the scattering wave is concentrated in the backward direction as shown in **Figure 8(c)**. Among the maximum value and the minimum value of asymmetry parameter, we find $\langle cos\Theta \rangle \approx 0$ at $x = 0.498980$, which means the scattering is symmetric with respect to the plane $z = 0$.

Hence, Fano resonances in core-shell particles can be used to detect the slight changes of core permittivity since they are sensitive in both magnitude and direction.

4. Fano resonances in arbitrary objects with high-permittivity dielectric

When the structure gets more complicated, the Mie theory is no longer valid for the solution of scattering field. We have to use the temporal coupled-mode theory (TCMT) to replace Mie

theory when investigating the Fano resonances in arbitrary objects with high-permittivity dielectric.

4.1. Temporal coupled-mode theory

The temporal coupled-mode theory provides a useful general framework to study the interaction of a resonance with external waves. It has been well developed when dealing with particles that have cylindrical or spherical shapes [21]. In [22], TCMT has been generalized to analysis the scattering of arbitrary shape structures. The temporal coupled-mode equations can be expressed as [23]

$$\begin{cases} \dfrac{dA}{dt} = \left(-i\omega_0 - \dfrac{1}{\tau}\right)A + \boldsymbol{\kappa}^T \boldsymbol{s}^+ \\ \boldsymbol{s}^- = \boldsymbol{B}\boldsymbol{s}^+ + A\boldsymbol{d} \end{cases} \tag{16}$$

In Eq. (16), $|A|^2$ corresponds to the energy inside the resonator. $\boldsymbol{s}^+$ and $\boldsymbol{s}^-$ represent incoming waves and outgoing waves, respectively. They couple directly by the resonant mode A is coupled with the outgoing waves $\boldsymbol{s}^-$ through $\boldsymbol{d}$ and is excited by the incoming waves $\boldsymbol{s}^+$ through $\boldsymbol{\kappa}^T$. ω_0 is the resonance frequency and $\frac{1}{\tau}$ is the external leakage rate.

There exists some constrains between $\boldsymbol{B}$, $\boldsymbol{d}$, and $\boldsymbol{\kappa}$, which are imposed by energy conservation and time-reversal invariance [22]. The constrain conditions are

$$\begin{cases} |\boldsymbol{d}|^2 = \dfrac{2}{\tau} \\ \boldsymbol{\kappa}^T \boldsymbol{d}^* = \dfrac{2}{\tau} \\ \boldsymbol{B}\boldsymbol{d}^* + \boldsymbol{d} = 0 \end{cases} \tag{17}$$

For a 2D arbitrary object, we can expand scattering field into cylindrical waves

$$H_{sca} = \sum_{m=-\infty}^{\infty} H_0 \; a_m \; H_{|m|}^{(1)}(k\rho) e^{im\theta} \tag{18}$$

$\boldsymbol{s}^+$ and $\boldsymbol{s}^-$ in Eq. (16) can be viewed as coefficients of input wave and outgoing wave on the basis of cylindrical waves.

The incident plane wave can also be expanded into cylindrical waves

$$e^{ikr} = \sum_{m=-\infty}^{\infty} i^{|m|} e^{-i\theta_0 m} \left(\frac{H_{|m|}^{(1)}(k\rho) + H_{|m|}^{(2)}(k\rho)}{2} \right) \times e^{i\theta m} \tag{19}$$

where θ_0 is the incident angle. Combined with cylindrical wave expansion, we can use TCMT to describe the Fano resonances in arbitrary objects with high-permittivity dielectric.

4.2. Numerical simulation

The method we determine the coefficients in Eq. (16) is similar to the method described in [22]. Firstly, we use eigenmode analysis in COMSOL 5.0 to figure out the resonance frequency ω_0 and the external leakage rate $\frac{1}{\tau}$. Secondly, being different from the method in [22] where they set $\boldsymbol{B} = \boldsymbol{I}$, we calculate the $\boldsymbol{B}$ through the simulation results of the arbitrary object covered by PEC illuminated by the plane wave. Since the slow varying background of high-permittivity sphere is the PEC sphere as mentioned above, it is intuitive to assume the slow varying background of arbitrary object which is described by $\boldsymbol{B}$ is the same as the object covered by PEC. Thirdly, combined with the field distribution of eigenmode simulation and background scattering matrix $\boldsymbol{B}$, we can figure out the resonant radiation coefficients $\boldsymbol{d}$. At last, $\boldsymbol{\kappa}$ can be solved through constrain conditions in Eq. (17).

Once the coefficients in Eq. (16) are determined, we can use the TCMT to predict the scattering fields by different incident frequencies and incident angles.

As shown in **Figure 9**, the relative permittivity of rounded-corner triangle is 600. The structure has a resonance frequency of $\omega_0 = 0.12172\omega_p$ and the leakage rate is $\frac{1}{\tau} = 1.1771 \times 10^{-4}$, which can be figured out by COMSOL. We use Matlab to set the temporal coupled-mode model as shown in Eq. (16). By comparing with the simulation results of COMSOL at different incident frequencies (near the resonance frequency) and incident angles, we can prove the validity of TCMT.

When a TM wave impinges on the scatterer, the scattering cross section can be defined as

$$C_{sct} = \frac{P_{sct}}{I_0} \tag{20}$$

where P_{sct} is the rate at which energy is scattered across the circle far away from the scatterer and $I_0 = \frac{1}{2}\sqrt{\frac{\mu_0}{\epsilon_0}}|H_0|^2$ is the intensity of the incident plane wave. For TCMT, the scattering cross section can be calculated by [22]

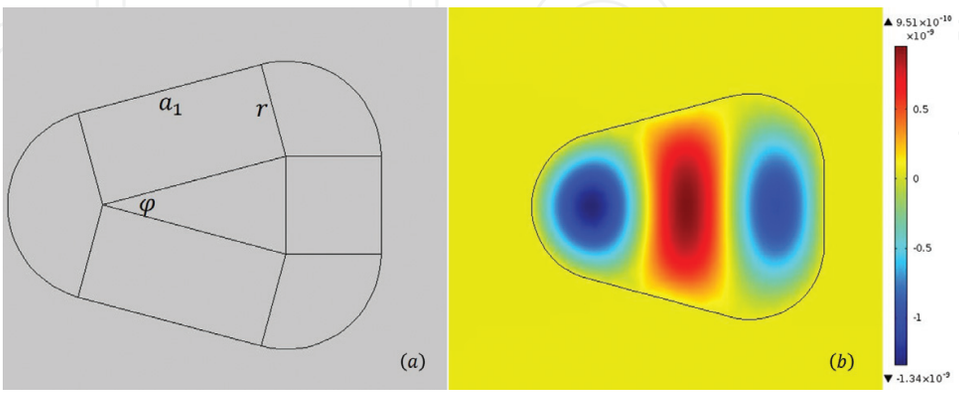

Figure 9. (a) Rounded-corner triangle with $r = 0.15\lambda_p, a_1 = 0.3\lambda_p, \phi = \frac{\pi}{6}, \epsilon = 600$. (b) The real part of H_z for the eigenmode analysis at the frequency $\omega_0 = 0.12172\omega_p$.

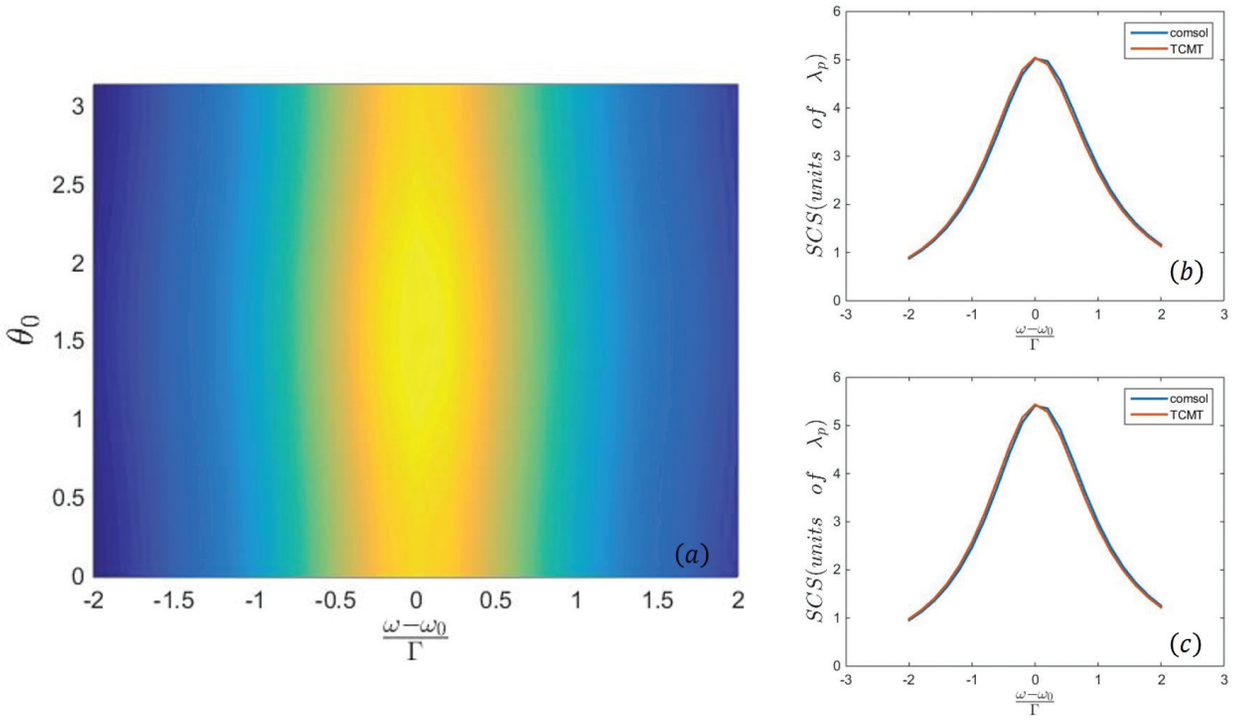

Figure 10. (a) Scattering cross section predicted by TCMT as a function of incident frequency ω and incident angle θ_0. Comparison between TCMT and COMSOL simulation results for different incident angles $\theta_0 = 0$ (b) and $\theta_0 = \frac{\pi}{2}$ (c).

$$C_{sct} = \frac{((\boldsymbol{S} - I)\boldsymbol{s}^+)^\dagger (\boldsymbol{S} - I)\boldsymbol{s}^+}{I_0} \tag{21}$$

where

$$\mathbf{S} = \mathbf{B} + \frac{\boldsymbol{d}\boldsymbol{\kappa}^T}{i\omega_0 - i\omega + \frac{1}{\tau}} \tag{22}$$

As shown in **Figure 10(b, c)**, for different incident angles, scattering cross sections predicted by TCMT match well with the results simulated by COMSOL.

As shown in **Figure 11**, the green line represents the assumption in [22] that the background scattering matrix $\boldsymbol{B}$ can be set to $\boldsymbol{I}$ while the blue line represents the assumption that $\boldsymbol{B}$ is achieved through the simulation results of the arbitrary object covered by PEC. As we can see, when the incident frequency equals to the resonance frequency, both the green line and blue line (TCMT models with different parameters) can match the simulation results. However, when the incident frequency deviates from the resonance frequency, our TCMT model shows a better accuracy compared with the TCMT model in [22], which indicates that the background scattering matrix $\boldsymbol{B}$ cannot be set to $\boldsymbol{I}$ easily when the permittivity of object is high.

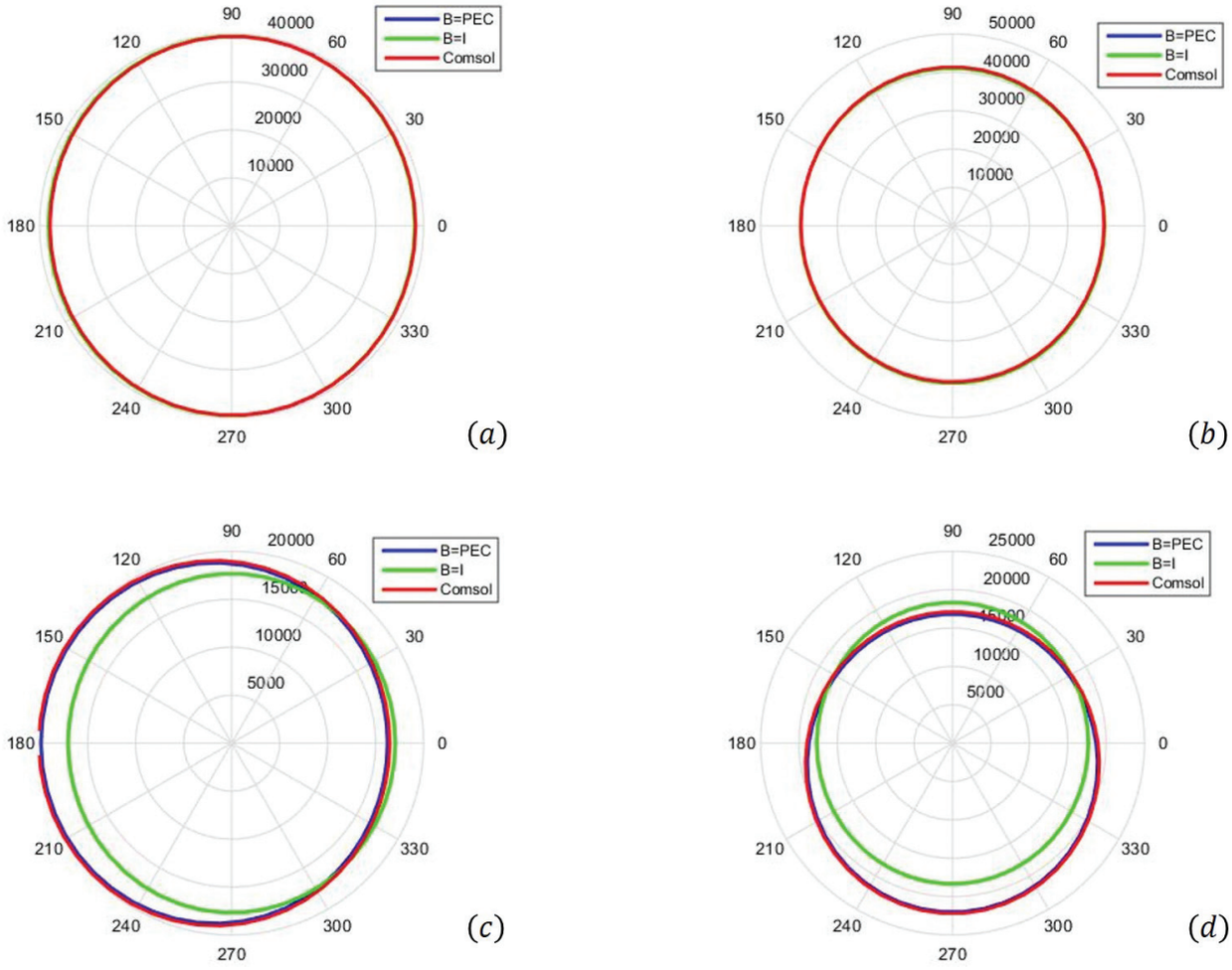

Figure 11. The far-field amplitude of the scattering field with different incident frequencies and angles of (a) $\omega = \omega_0$, $\theta_0 = 0$, (b) $\omega = \omega_0$, $\theta_0 = \frac{\pi}{2}$, (c) $\omega = \omega_0 + 2\Gamma$, $\theta_0 = 0$, (d) $\omega = \omega_0 + 2\Gamma$, $\theta_0 = \frac{\pi}{2}$.

5. Fano resonances in periodic structures

Fano resonances have been widely observed in the various periodic structures [24, 25]. The theory of Fano resonance in periodic structures is well developed. In [26], temporal coupled-mode theory is applied to analysis the transmission spectra of photonic crystal slab. According to the TCMT, the Fano resonances existed in transmission spectra are the result of the coupling of leaky mode to the external waves. Recently, the experimental discovery of Fano resonances involving interference between Mie scattering and Bragg scattering is studied in [27]. By comparing the disordered system with the periodic structure, they conclude the sharp resonances in periodic structure are caused by the Bloch waves. In order to study the interference between Mie scattering and Bragg scattering theoretically, the inverse dispersion method is proposed to calculate the photonic band diagram and distinguish unambiguously between Bragg and Mie gaps in the spectra [28]. The method reduces Maxwell's equations to a problem with the eigenvalue k while ω is considered to be a real parameter. It is not so intuitive since conventional approach will reduce the Maxwell's equations to standard eigenproblem for the

frequency [29]. In [30], the author shows that the frequencies of observed Fano resonances existed in a linear array of dielectric cylinders coincide with the position of narrow frequency bands found in the spectra of corresponding two-dimensional photonic crystals. Inspired by [28, 30], we figure out the eigenfrequency of the photonic crystal slab and compare with the band diagram of two-dimensional photonic crystal. We are surprised to find that the occurrence of Fano resonances in photonic crystal slab can be predicted by the band diagram of photonic crystal.

5.1. Transmission spectra of the photonic Crystal slab

The structure of photonic crystal slab is shown in **Figure 12**. We assume the dielectric cylinders are parallel to the z axis. When TE waves with different angles incident on the slab, we can calculate the transmission coefficients and plot them in **Figure 13**.

As shown in **Figure 13**, Fano resonances with narrow resonance width can be observed. The permittivity of photonic crystal slab does not need to be as high as single cylinder in order to achieve same quality factor and such materials may be easily found in nature.

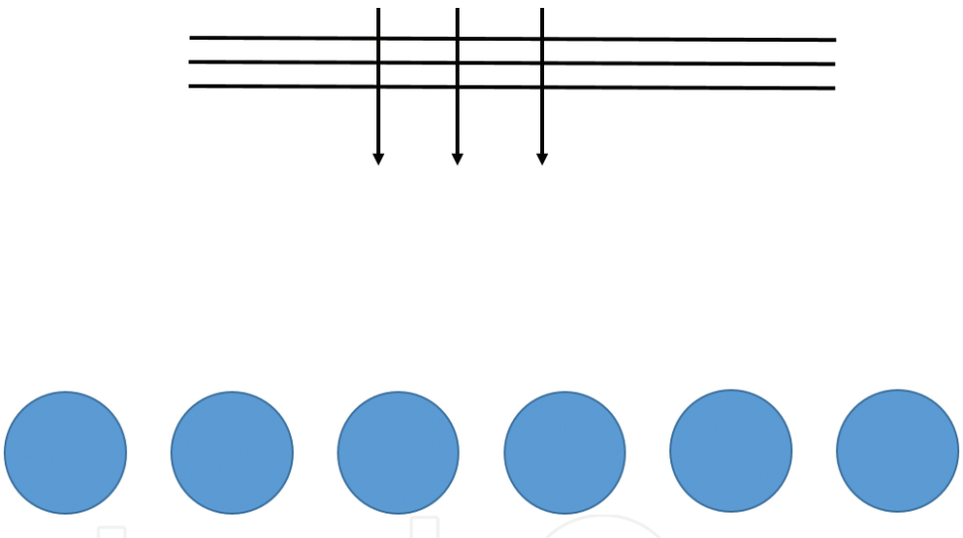

Figure 12. Photonic crystal slab with radius of cylinders $r = 0.4a$ (a is the period of the slab), $\epsilon = 12$, $\mu = 1$.

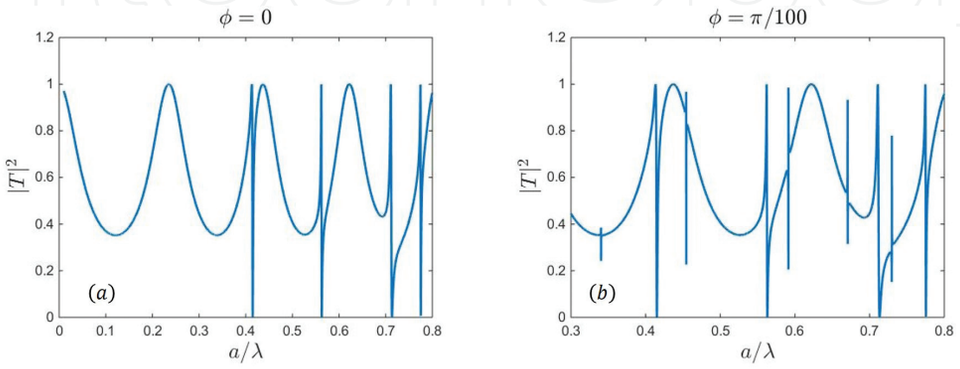

Figure 13. Transmission coefficient of plane wave incident on the photonic crystal slab. The incident angles are (a) $\varphi = 0$ and (b) $\varphi = \frac{\pi}{100}$.

Let us assume the Fano resonances in **Figure 13** satisfy the Fano function $\frac{1}{1+q^2}\frac{\left(q+\frac{\omega-\omega_0}{\Gamma}\right)^2}{1+\left(\frac{\omega-\omega_0}{\Gamma}\right)^2}$. Firstly, we use eigenmode analysis in COMSOL to figure out the eigenfrequency of photonic crystal slab. The real and imaginary part of eigenfrequency represent the resonance frequency ω_0 and resonance width Γ respectively. Secondly, we use the fitting method in Matlab to get the optimal Fano parameter q in Fano function. Thirdly, with given ω_0, Γ, and q, we can plot the Fano function with respect to frequency ω. As shown in **Figure 14**, the Fano curve matches well with the transmission coefficient simulated by COMSOL. The horizontal ordinate is chosen as a/λ for convenience, which is proportional to frequency ω.

5.2. Band diagram of photonic Crystal

The photonic crystal slab is periodic in only one direction while two-dimensional photonic crystal is periodic in two directions. For a photonic crystal as shown in **Figure 15**, the band diagram for $k_y = 0, 0 \le k_x \le \frac{\pi}{a}$ is plotted in **Figure 16(a)**. The eigenfrequencies of the photonic crystal are real while the eigenfrequencies of the photonic crystal slab are complex due to the existence of radiation loss. Hence, only the real parts of eigenfrequencies are plotted as shown in **Figure 16(b)**. By comparing the resonance frequencies shown in **Figure 13** and eigenfrequencies in **Figure 16(b)**, we can conclude that the occurrence of Fano resonances in transmission spectra of photonic crystal slab can be predicted by the real parts of the eigenfrequencies of the system. In addition, for the Fano resonances, which are observed in **Figure 13(b)** but cannot be observed in **Figure 13(a)**, they all have the eigenfrequencies with $Q \to \infty$. Hence, the resonance widths tend to zero and the resonances cannot be observed.

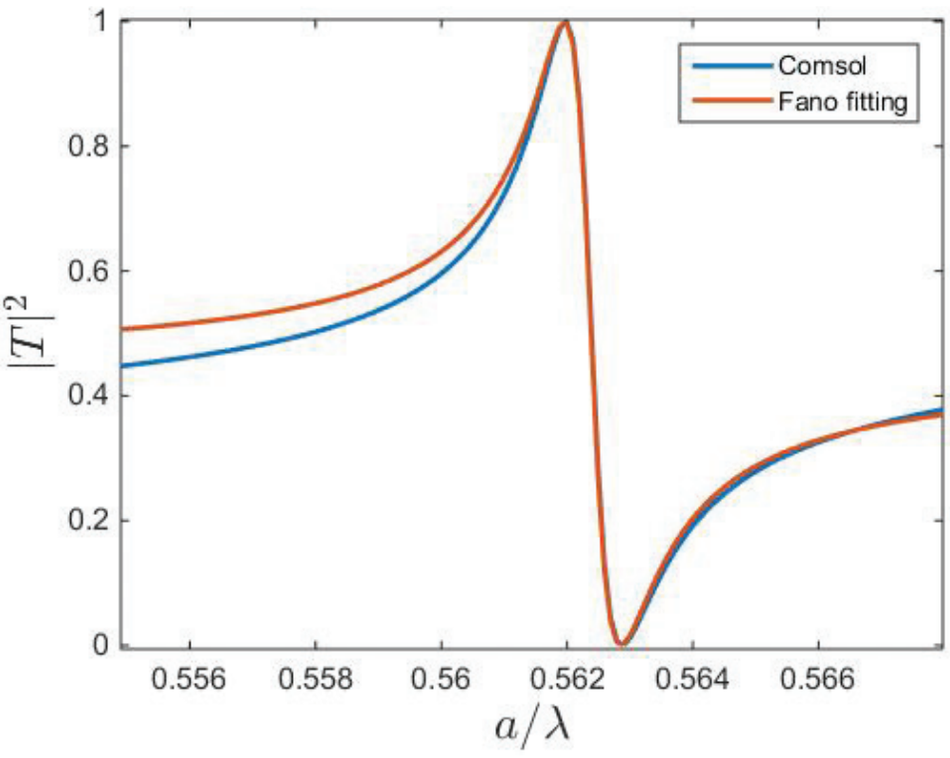

Figure 14. The Fano curve and the simulation result of photonic crystal slab are plotted.

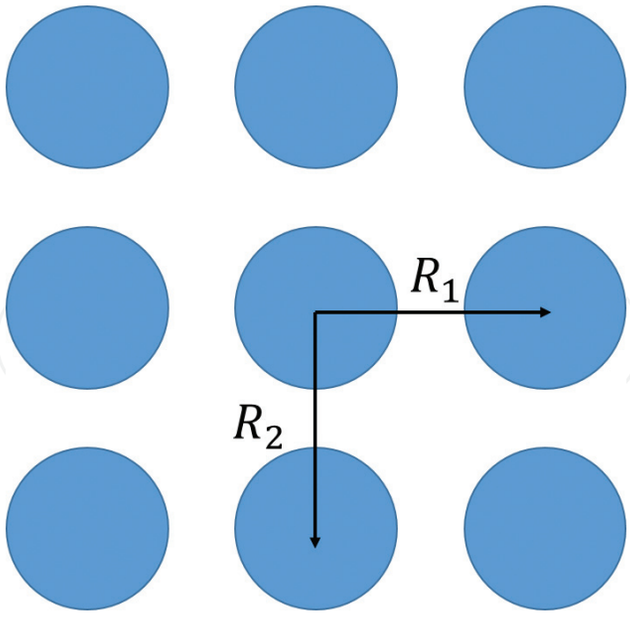

Figure 15. Photonic crystal with radius of cylinders $r = 0.4a$ ($R_1 = R_2 = a$), $\epsilon = 12$, $\mu = 1$.

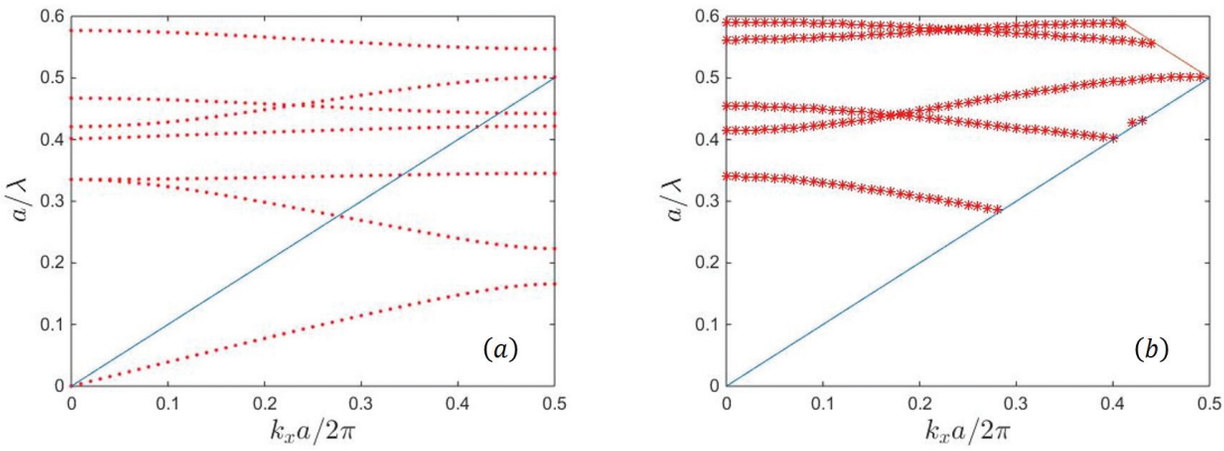

Figure 16. (a) Band diagram of two-dimensional photonic crystal as shown in **Figure 15** when $k_y = 0, 0 \leq k_x \leq \frac{\pi}{a}$. (b) Real parts of eigenfrequencies of photonic crystal slab as shown in **Figure 12** with $Q > 70$ are plotted.

As shown in **Figure 16**, the Fano resonances of the transmission spectra coincide with the band diagram of the two-dimensional photonic crystal, which further explains that Fano resonances in periodic structures can be viewed as the superposition of the Bloch wave, which provides the narrow resonances and the Mie scattering wave which provides the slow varying background.

6. Conclusion

In this chapter, we have presented various structures with high permittivity, which have Fano resonances, such as spheres, core-shell particles, arbitrary shape objects, and periodic

structures. For each structure, different theoretical methods together with numerical analysis have been presented. Compared with conventional Fano resonances observed in structures consisted of metal and dielectric, high-permittivity structures can enhance the quality factor significantly, which may open up new opportunities for applications such as sensors, switches, and permittivity measuring technique.

Author details

Xianghong Kong*, Lina Qiu and Gaobiao Xiao

*Address all correspondence to: klovek@sjtu.edu.cn

Department of Electronic Engineering, Shanghai Jiao Tong University, China

References

[1] Fano U. Effects of configuration interaction on intensities and phase shifts. Physical Review. 1961;**124**:1866-1878. DOI: 10.1103/PhysRev.124.1866

[2] Wood RW. On a remarkable case of uneven distribution of light in a diffraction grating Spectrum. Proceedings of the Physical Society of London. 1902;**18**:269-275. DOI: 10.1088/1478-7814/18/1/325

[3] Hao F, Sonnefraud Y, Van Dorpe P, Maier SA, Halas NJ, Nordlander P. Symmetry breaking in plasmonic nanocavities: Subradiant LSPR sensing and a tunable Fano resonance. Nano Letters. 2008;**8**(11):3983-3988. DOI: 10.1021/nl802509r

[4] Luk'yanchuk B, Zheludev NI, Maier SA, Halas NJ, Nordlander P, Giessen H, et al. The Fano resonance in plasmonic nanostructures and metamaterials. Nature Materials. 2010;**9**(9):707-715

[5] Jahani S, Jacob Z. All-dielectric metamaterials. Nature Nanotechnology. 2016;**11**(1):23-26

[6] Bohren CF, Huffman DR. Absorption and scattering by a sphere. In: Absorption and Scattering of Light by Small Particles; 2004. p. 82-129

[7] Foteinopoulou S, Vigneron JP, Vandenbem C. Optical near-field excitations on plasmonic nanoparticle-based structures. Optics Express. 2007;**15**:4253-4267

[8] Yannopapas V, Moroz A. Negative refractive index metamaterials from inherently non-magnetic materials for deep infrared to terahertz frequency ranges. Journal of Physics. Condensed Matter. 2005;**17**:3717-3734

[9] Rybin MV, Filonov DS, Belov PA, Kivshar YS, Limonov MF. Switching from visibility to invisibility via Fano resonances: Theory and experiment. Scientific Reports. 2015;**5**:8774

[10] Kong X, Xiao G. Fano resonance in high-permittivity dielectric spheres. Journal of the Optical Society of America. A. 2016;**33**(4):707-711

[11] Arruda TJ, Martinez AS, Pinheiro FA. Unconventional Fano effect and off-resonance field enhancement in plasmonic coated spheres. Physical Review A. 2013;**87**:043841

[12] Arruda TJ, Martinez AS, Pinheiro FA. Tunable multiple Fano resonances in magnetic single-layered core-shell particles. Physical Review A. 2015;**92**:023835

[13] Kong X., Xiao G. Fano resonances in core-shell particles with high permittivity covers. In: Progress in Electromagnetic Research Symposium (PIERS); IEEE. 2016. pp. 1715–1719.

[14] Zheng G, Chen Y, Bu L, Xu L, Su W. Waveguide-coupled surface phonon resonance sensors with super-resolution in the mid-infrared region. Optics Letters. 2016;**41**(7):1582-1585

[15] Rahmani M, Luk'yanchuk B, Hong M. Fano resonance in novel plasmonic nanostructures. Laser and Photonics Reviews. 2013;**7**(3):329-349

[16] Zafar R, Salim M. Enhanced figure of merit in Fano resonance-based plasmonic refractive index sensor. IEEE Sensors Journal. 2015;**15**(11):6313-6317

[17] Chen H, Shao L, Man YC, Zhao C, Wang J, Yang B. Fano resonance in (gold core)-(dielectric shell) nanostructures without symmetry breaking. Small. 2012;**8**(10):1503-1509

[18] Raschke G, Brogl S, Susha A, Rogach A, Klar T, Feldmann J, et al. Gold nanoshells improve single nanoparticle molecular sensors. Nano Letters. 2004;**4**(10):1853-1857

[19] Fan X, Zheng W, Singh DJ. Light scattering and surface plasmons on small spherical particles. Light: Science & Applications. 2014;**3**(6):e179

[20] Mishchenko MI, Travis LD, Lacis AA. Scattering, Absorption, and Emission of Light by Small Particles. Cambridge, England: Cambridge University Press; 2002. p. 486

[21] Ruan Z, Fan S. Temporal coupled-mode theory for Fano resonance in light scattering by a Sinble obstacle. Journal of Physical Chemistry C. 2010;**114**(16):7324-7329

[22] Ruan Z, Fan S. Temporal coupled-mode theory for light scattering by an arbitrarily shaped object supporting a single resonance. Physical Review A. 2012;**85**:043828

[23] Haus HA. Waves and Fields in Optoelectronics. Upper Saddle River, New Jersey: Prentice-Hall; 1984. p. 748

[24] Kanskar M, Paddon P, Pacradouni V, Morin R, Busch A, Young JF, et al. Observation of leaky slab modes in an air-bridged semiconductor waveguide with a two-dimensional photonic lattice. Applied Physics Letters. 1997;**70**:1438-1440

[25] Astratov VN, Culshaw IS, Stevenson RM, Whittaker DM, Skolnick MS, Kraus TF, et al. Resonant coupling of near-infrared radiation to photonic band structure waveguides. Journal of Lightwave Technology. 1999;**17**:2050-2057

[26] Fan S, Suh W, Joannopoulos JD. Temporal coupled-mode theory for the Fano resonance in optical resonators. Journal of the Optical Society of America. A. 2003;**20**(3):569-572

[27] Rybin MV, Khanikaev AB, Inoue M, Samusev KB, Steel MJ, Yushin G, et al. Fano resonance between Mie and Bragg scattering in photonic crystals. Physical Review Letters. 2009;**103**(2):023901

[28] Rybin MV, Limonov MF. Inverse dispersion method for calculation of complex photonic band diagram and PT symmetry. Physical Review B. 2016;**93**:165132

[29] Joannopoulos JD, Johnson SG, Winn JN, Meade RD. Photonic Crystals: Molding the Flow of Light. 2nd ed. Princeton: Princeton University Press; 2008

[30] Markos P. Fano resonances and band structure of two-dimensional photonic structures. Physical Review A. 2015;**92**:043814